https://doi.org/10.1016/j.intermet.2017.12.004

Deformation behavior of bulk metallic glasses under a mixed-mode (I/II) loading condition

S.H. Chen[1,2*], A. Domel[3], T.M. Yue[2], C.P. Tsui[2], K.C. Chan[2], K.A. Dahmen[3], and P.K. Liaw[4]

[1]School of Mechanical Engineering, Hefei University of Technology, Hefei 230009, China.

[2]Advanced Manufacturing Technology Research Centre, Department of Industrial and Systems Engineering, The Hong Kong Polytechnic University, Hung Hom, Kowloon, Hong Kong.

[3]Department of Physics, University of Illinois, Urbana-Champaign, Illinois 61801, USA.

[4]Department of Materials Science and Engineering, The University of Tennessee, Knoxville, TN 37996, USA.

*Corresponding author. E-mail: shchen@hfut.edu.cn

Abstract

Bulk metallic glasses (BMGs) demonstrate different deformation behavior under varying loading conditions. In the present work, a $Zr_{57}Cu_{20}Al_{10}Ni_8Ti_5$ (atomic percent, at.%) BMG was subjected to a mixed-mode (I/II) loading condition by tailoring double-side notches. The findings show stable plastic-flow plateau stages in the loading-displacement curves, and this phenomenon is different from other notched BMG specimens with predominant-mode-I failure. More importantly, due to the stress concentrations between two notches, most of the slip events with large load drops occur on the fracture plane, resulting in a wide smooth region consisting of several shear steps on the fracture surface. We show that despite different deformation behavior, the specimens still display slip-size statistics of the plastic flow, which are similar to those seen in compression tests. The present findings give more insight into the deformation behavior/mechanisms of BMGs under varying loading conditions for practical structural applications.

Key words: Bulk metallic glass; Deformation behavior; Stress gradient; Loading condition.

1. Introduction

Without crystalline lattices, bulk metallic glasses (BMGs) are known to have many attractive properties, such as a large elastic limit of 2% [1,2], high strength approaching the ideal values [2], good biocompatibility and corrosion resistance [3], excellent magneto-caloric effect [4,5], and high processing capability [6]. During past two decades, many efforts have been devoted to developing and commercializing BMGs, and they are now poised for practical structural applications [7]. Due to the amorphous atomic arrangements, the plastic deformation in BMGs at room temperature is localized in thin layers of shear bands [8,9], and the macroscopic deformation behavior is different under varying loading conditions. For example, under compression tests, they display a wide range of plasticity on the change of alloy compositions [10,11], sample sizes [12,13], and loading rates [14,15]. Under tension, almost all specimens exhibit brittle fracture behavior by the rapid propagation of shear bands, where very limited ductility can be achieved [16]. Some studies have shown that under mixed-mode (I/II) loading conditions under bending, BMGs are able to demonstrate higher fracture toughness [17,18], and the increase in the mode-II component can increase the plastic-zone size ahead of the crack tips [19]. It is vital to understand the deformation behavior of BMGs under varying loading conditions before their widespread structural applications in industry.

In a recent work, delayed catastrophic failures in BMGs have been achieved by tailoring complex stress fields through double-side notches, where the specimens also deform under a mixed-mode (I/II) loading conditions [20]. Although the deformation behavior of BMGs under mixed mode loading conditions has been widely reported [17-23], the deformation features of BMGs under the mixed-mode (I/II) loading condition as shown in Ref. [20] have not been fully understood, where the mode II

component plays a dominant role. Such a mixed-mode (I/II) loading condition is different from the predominant-mode-II fracture under compression [24,25], the mixed-mode (I/II) loading condition under bending [17,19], the pure mode-II loading condition in the edge notched flexure specimens [26], or the predominant-mode-I failures of double-side-notched BMG specimens [27-29]. In the present work, the deformation behavior of a BMG under such a mixed-mode (I/II) loading condition, including fracture-surface features and plastic-flow dynamics, has been examined under varying loading rates.

2. Experimental

As-cast BMG rods with a nominal composition of $Zr_{57}Cu_{20}Al_{10}Ni_8Ti_5$ (atomic percent, at.%) were fabricated by copper-mould casting from pure elements [30]. The amorphous atomic structure of the as-cast specimens was checked, using the standard X-ray diffraction (XRD) analysis on a Rigaku SmartLab X-ray diffractometer. Double-side-notched BMG specimens were designed as shown in **Figure 1**a [20] and fabricated from the as-cast rods, and the notches were cut, using a diamond saw. Figure 1b presents an example of the prepared specimens. Mechanical tests were conducted on an Instron 5565 materials testing machine at loading rates of 0.3, 0.06, and 0.012 mm/min., respectively, and more detailed information was described in Ref. [20]. Three specimens were tested for repeatability. After mechanical testing, the sample surfaces and fracture morphologies were inspected, using a Jeol JSM-6490 scanning electron microscope. To characterize the stress distribution around the notches, finite-element-modelling (FEM) analysis was conducted, employing a commercial ABAQUS package [20]. An ideal elastic-plastic constitutive model was used for the FEM analysis [31,32], and the input parameters for the BMG are 1.635 GPa for the yield stress [33], 82 GPa for the Young's modulus [34], and 0.36 for the Poisson's ratio [34].

3. Results

3.1 Mechanical-testing results

The load-axial displacement curves of the notched BMG specimen are given in **Figure 2**a. It can be seen that the specimens display a plastic-flow plateau stage of serration flows at all loading rates. The load drops (Δf) in the curves (Fig. 2a inset) indicate the release of the elastic energy during the loading process [35,36], which are usually related to the formation and propagation of shear bands [37,38]. The displacement ranges for the plastic flows before failure (w_p) are 0.070 ± 0.003, 0.066 ± 0.004, and 0.079 ± 0.009 mm for loading rates of 0.30, 0.06, and 0.012 mm/min., respectively. As compared with the notched BMG specimens with a predominant-mode-I failure [29], the present specimens demonstrate more plastic flows (load drops), especially for the occurrence of the plastic-flow plateau stages. After fracture, the specimens display similar morphologies on the side surfaces at all loading rates. **Figure 3**a shows the surface morphology of a typical fractured specimen at a loading rate of 0.06 mm/min., where the specimen fractured at an angle of $\theta \approx 27°$. In the region, **N**, between two notches (Figs. 3a,d), only one shear band along the fracture-plane direction was observed. The maximum normal stress component (σ_n) and shear stress component (τ) of present mixed-mode loading condition were estimated and compared with tensile results of the same BMG as shown in Ref. [39]. The results show that the normal stress component under present mixed-mode loading condition (516 MPa) is much smaller than the value under tension (1256 MPa), while the shear stress component (1012 MPa) is larger than the value under tension (880 MPa). This has further confirmed that the shear stress component plays a dominant role in the mixed-mode loading condition, resulting in different deformation behavior.

At the notch root (the region, **M**, in Figs. 3a,c), a shear-band region was also observed. However, these shear bands have directions nearly perpendicular to the loading directions and cannot cause the final failures. In Ref. [20], it has been shown that the shear bands in the region, **M**, may result in the formation of load drops less than 5 N in the load-axial displacement curves. Two stages of the plastic flow were, then, determined by the first occurrence of a load drop larger than 5 N (Δf_1), as shown in Fig. 2b. The widths of the displacement ranges for the plastic flows in stage II (w_{pII})

are, then, measured as 0.065 ± 0.004, 0.058 ± 0.005, and 0.076 ± 0.009 mm for loading rates of 0.30, 0.06, and 0.012 mm/min., respectively. According to Ref. [20], the stage II of the plastic flow should be related to the formation of shear bands along the fracture-plane direction, as presented in the region, **N** (Fig. 3). The observation of just one shear band in this region suggests that the slip events relating to the load drops at the stage II may mainly occur on the fracture plane, resulting in the formation of a shear offset (δ_s), as shown in the schematic diagram in Fig. 3b. After fracture, the shear offset (δ_s) can be estimated as

$$\delta_s = d_w/\cos(\theta) \quad (1)$$

If we use the width of the stage II to replace the axial displacement, i.e., $d_w = w_{pII}$, the shear offset of the whole specimen can be estimated as

$$\delta_s = w_{pII}/\cos(\theta) \quad (2)$$

The shear offsets of these specimens were, then, estimated as 73 ± 5 μm, 65 ± 6 μm, and 85 ± 10 μm for loading rates of 0.30 mm/min., 0.06 mm/min., and 0.012 mm/min., respectively.

The formation of shear bands in the notched specimen can be related to the stress concentrations around the notches. As shown in **Figure 4a**, the FEM results of the Mises-stress distributions show that the stress concentration regions will firstly appear in the region, **M**, and tend to penetrate the region, **N**. It can, then, be speculated that under applied loadings, shear bands firstly initiate in the region, **M** (Fig. 3c) and cause the small load drops at the stage I of the plastic flow (Fig. 2b). When the loading process proceeds, the shear bands near the fracture plane propagated to the region, **N**, leading to the slip events with larger load drops at the stage II (Fig. 2b). This can be verified by the penetration of the yielded regions in Fig. 4b. Due to the stress concentration along two notches (Fig. 4b), the slip events were mainly confined to occur on the fracture plane, resulting in the shear offset (Fig. 3b) and few shear bands in the region, **N** (for example, just one shear band was observed besides the fracture plane in Fig. 3d). It should be pointed out that the change of mode mixity will affect the formation of shear bands and result in varying plastic deformation behavior [40].

According to the equation $M^e = (2/\pi)\tan^{-1}(\sigma_n/\tau)$ [40], the mixity of the present predominant-mode-II loading condition can be calculated as 0.3, where $M^e = 1$ and 0 denotes pure mode I and pure mode II loading conditions, respectively. In our previous work, the effect of increasing mode I component on the plastic deformation behavior of the notched BMG specimens has been examined [20]. Thus in this paper, we mainly focus on the deformation behavior of the BMG on such a predominant-mode-II loading condition.

3.2. Fracture-surface observations

Similar to the crystalline alloys, the fracture-surface features of BMGs also play an important role in revealing the deformation and fracture mechanisms of BMGs, and have been examined extensively [24,27,39,41-47]. The fracture process of BMGs consists of a shear process by the propagation of shear bands, following a separation process of two solid parts, where a fluid layer was formed between two solid parts before separation [24,42,44]. The fracture-surface features of BMGs are significantly dependent on the loading conditions [24,43] and stress states [39,45]. Our further examinations of the fracture morphologies have shown that all specimens have similar fracture-surface features at varying loading rates. **Figure 5** presents the typical fracture-surface features of a specimen at a loading rate of 0.012 mm/min. The fracture surface of the specimen has three kinds of typical patterns: ridge-like vein patterns coexisting with diamond-shaped smooth cores (Figs. 5b,d), cell-like vein patterns (Fig. 5c), and smooth regions consisting of several shear steps (Fig. 5e). The smooth regions are formed during the shear process before the separation of two solid parts [24,42,44], and are in line with the shear offset in Fig. 3b. On the one hand, several shear steps in the smooth regions (Fig. 5e) agree well with the slip events containing large load drops at the stage II of the plastic flow (Fig. 2a).

In conventional tensile tests of BMGs with a mode-I failure, a smooth region without steps was formed due to the rapid propagation of a shear band [24,27]. In contrast, in the present work, due to the confinement of the stress concentration between two

notches, most slip events at stage II occur on the fracture plane, resulting in several steps in the smooth regions. On the other hand, the widths of the smooth regions in the present specimens, for example, 66 μm in Fig. 5, are larger than the value in conventional tensile tests (about 42 μm) [39], indicating the occurrence of more slip events on the fracture plane. For the specific specimen in Fig. 5, the width of the displacement range for the stage-II plastic flow, w_{pII} = 67 μm. The shear offset can, then, be estimated as $\delta_s = w_{pII}/\cos(\theta)$ = 75 μm, which is slightly larger than the SEM observation (66 μm). Besides the fracture plane, few shear bands are observed along the fracture-plane direction in the region, **N** (see an example in Fig. 3d), which also accommodated some slip events at the stage II of the plastic flow. Thus, it is reasonable to find that the calculated value based on the assumption that all slip events occur on the fracture plane (Fig. 3b) is slightly larger than the SEM observation on the fracture surface.

After the formation of the smooth region, other fracture-surface features were formed during the separation of two solid parts. The radiating veins coexisting with smooth cores are usually observed on the fracture surface of conventional tensile specimens with the mode-I failure [24,27]. However, under the present mixed-mode (I/II) loading condition, the ridge-like vein patterns show some differences. It can be seen in Fig. 5, most of the ridges propagate along the shear direction, and the length of the ridges against the shear direction is much smaller than the length along the shear direction (Figs. 5b,d). This phenomenon is in line with the mixed-mode (I/II) fracture process that shearing plays a dominant role. In addition, the diamond-shaped smooth cores are usually observed on the tensile side of the bending specimens, where the mode-II failure plays a significant role [39]. Therefore, the formation of the radiating vein coexisting with diamond-shaped smooth cores could be the results of a fracture process with both modes I and II components. The formation of other ridge-like vein patterns relatively far from the diamond-shaped smooth cores, as shown in Fig. 5b, should be the result of normal stress effect. Besides the fracture-surface features similar to the conventional tensile tests, some cell-like vein patterns are also observed

(Fig. 5c), similar to the compression tests of BMGs with the predominant-mode-II failure [24]. Clear boundaries of the cell-like vein patterns have been observed in Fig. 5c, implying that the cell-like vein patterns may form at an individual shear process, where the mode-II failure plays a dominant role. The formation of the fracture-surface features are, then, summarized in a schematic diagram in **Figure 6**. Under applied loadings, smooth regions are firstly formed at a mode-II fracture process by shearing, where no separation of the solid parts occurs (Fig. 6a). Then the two solid parts separate partially under a combined effect of both mode-I and II components, resulting in the formation of the ridge-like vein patterns, and radiating veins coexisting with diamond-shaped smooth cores. At this stage, some fluids may not be fully separated, but assemble to several regions (Fig. 6b) due to the Tailor instability [24,42,44]. Finally, the specimen is fully separated at a mode-II fracture process, resulting in the formation of cell-like vein patterns, similar to the compressive testing results.

3.3 Mean-field interaction modelling of the serration behavior

The plastic flow in BMGs is characterized by intermittent bursts of stress/load drops, and the plastic-flow dynamics of the serrated plastic flow are important for understanding the deformation mechanisms as well as the delay of catastrophic failures of BMGs [20,35,48-51]. The plastic-flow dynamics under compression [48-50,52,53] and nano-indentations tests [54] have been studied extensively. Under mixed-mode loading conditions, it is shown that the change of mode mixity can be used to tune the criticality of the plastic-flow dynamics [20]. However, for the predominant-mode-II loading condition in the present work, it is still unknown about whether such a mixed-mode loading condition can affect the criticality of corresponding plastic-flow dynamics. In the present work, we show that although BMGs demonstrate different deformation behavior, as compared with the compression tests (predominant-mode-II failure) [24] and notched tensile tests (predominant-mode-I failure) [29], they still demonstrate slip-size statistics of the plastic flow similar to those seen in compression tests.

Based on a mean-field theory (MFT) [53,55], the corresponding complementary cumulative distribution of the load drop, L, in the serrated plastic flow can be expressed as

$$C(L) \sim L^{-(\kappa-1)} D_L(L/L_C) \quad (3)$$

where L_C is the exponentially-decaying cut-off load drop, κ is a power-law exponent, and $D_L(L/L_C)$ is a universal scaling function [53,56-60]. The MFT-modeling results of the serrated flow are given in **Figure 7**. It can be seen that at the loading rate of 0.012 mm/min., a noisy part was observed for the lowest slip sizes, whose distribution is consistent with the predicted distribution for brittle materials where the small avalanches should follow a power law distribution with an exponent of κ-1 = -1/2. The scaling exponent of κ-1 = 1/2 has been reported to be universal for the avalanches in solids from nanocrystals to earthquakes [56]. The present findings suggest that even with the change of the dominant loading conditions, the power-law scaling of the load drops in BMGs might also be universal. At the relatively-large load drops, the distribution does not have a power-law scaling [20], which is also consistent with the model predictions for brittle materials [61] and the compression tests of BMGs [62,63]. At higher loading rates (0.3 and 0.06 mm/min.), although the data become a bit more muddled, they are still qualitatively consistent with the model (Fig. 7). This muddle of the data may be due to that the distinction between small and large load drops is a bit mixed, and it is harder to analyze them separately.

The power-law critical dynamics of BMGs have been observed in conventional compression tests [35,53,64], compression tests with external disturbances [48,50,52], double-side-notched BMGs with complex stress fields [20] and nano-indentation tests [54]. Combining with the mixed-mode (I/II) condition in the present work, it seems that the change of the loading condition may not change the power-law critical dynamics in the plastic flow, except tension. Due to the brittle fracture nature of BMGs under tension, it is still challenging to study the plastic-flow dynamics of BMGs under tension, and is worthy of further investigations. Nevertheless, recent

work has shown that the plastic flow of flawed BMGs can still exhibit a power-law critical dynamics under tension [65]. The authors would like to mention that although a plastic-flow plateau stage has been obtained, the number of load drops is still small, as compared with the compressive-testing results of BMGs [53], or the specimens with delayed catastrophic failures [20]. The collection of more serration data might be useful for separating the muddled results of the BMG specimens at high strain rates.

4. Discussion

As a new class of structural materials, BMGs are poised for widespread structural applications in industry [7], where the materials deform under varying loading conditions. The present work uncovers the deformation behavior of a BMG under a mixed-mode (I/II) loading condition, providing guidance for the practical application of BMGs under varying loading conditions. We report for the first time that under a mixed-mode (I/II) loading condition, BMGs are able to demonstrate a stable plastic-flow stage, where most of the slip events occur on the fracture plane. This feature is different for the observations of one-to-one corresponding relationship between the shear bands and stress drops under compression tests [37]. These findings have further been validated by the observation of the fracture-surface features. The fracture morphologies reflect the combined effect of both normal and shear stress. The smooth regions and the cell-like vein patterns are mainly formed due to the shear stress effect; the ridge-like vein patterns may result from the normal stress effect; and the radiating veins coexisting with diamond-shaped smooth cores are formed under a combined effect of both normal and shear stress. The fracture morphology reveals a better understanding of the fracture process of the BMGs under varying loading conditions in practical applications [39]. Additionally, the findings suggest that the slip-size distributions in the plastic flow of the BMGs following the reported experiment are remarkably similar to the predictions of a simple mean field model [61] for un-notched BMGs that are compressed under uniaxial conditions (see Figure 7). Future experiments will test the detailed effects of the loading geometry on the serration statistics. The results could be useful for understanding the underlying deformation

mechanisms of BMGs and achieving stable plastic flows in BMGs by tailoring complex stress fields or loading conditions. As a promising class of structural materials, some BMG structures have demonstrated excellent mechanical performance [66-68]. The present findings may also be helpful for understanding the deformation mechanisms or developing BMG structures with unique mechanical properties, where the struts are always deform under varying/mixed loading conditions.

5. Conclusion

In summary, the deformation behavior of a Zr-based BMG under a mixed-mode (I/II) loading condition has been examined. The results show stable stages of plastic-flow plateaus in the load-axial displacement curves, which are different from the notched BMG specimens with the predominant-mode-I failures. Under such a mixed-mode (I/II) loading condition, most slip events with large load drops occur on the fracture plane, resulting in the formation of a wider smooth region with several steps, as compared with conventional tensile results. The deformation behavior as well as the fracture process has further been validated and discussed by examining the fracture-surfaces features. Moreover, despite different deformation behavior, the slip-size distributions are similar to those predicted by a mean field model [61] and measured uniaxial compression tests of un-notched samples [62,63]. The present findings give more insight into the deformation mechanisms of BMGs under varying loading conditions for practical structural applications.

Acknowledgements

SHC, TMY, and CPT thank the financial support of a grant from the Research Committee of the Hong Kong Polytechnic University (Research Project No. 1-YW0R). PKL would like to acknowledge the Department of Energy (DOE), Office of Fossil Energy, National Energy Technology Laboratory (DE-FE-0008855 and De-FE-0024054), with Mr. V. Cedro and Mr. R. Dunst as program managers. KAD and PKL

thank the support from the project of DE-FE-0011194 with the program manager, Dr. J. Mullen. PKL very much appreciate the support of the U.S. Army Research Office project (W911NF-13-1-0438) with the program manager, Dr.s M.P. Baker and D. M. Stepp. PKL thanks the support from the National Science Foundation (DMR-1611180) with the program director, Dr. D. Farkas.

References

[1] W.H. Wang, The elastic properties, elastic models and elastic perspectives of metallic glasses, Prog. Mater. Sci., 57 (2012) 487-656.

[2] A.R. Yavari, J.J. Lewandowski, J. Eckert, Mechanical properties of bulk metallic glasses, MRS Bull., 32 (2007) 635-638.

[3] Y. Liu, Y.M. Wang, H.F. Pang, Q. Zhao, L. Liu, A Ni-free ZrCuFeAlAg bulk metallic glass with potential for biomedical applications, Acta Biomater, 9 (2013) 7043-7053.

[4] L. Xia, C. Wu, S.H. Chen, K.C. Chan, Magneto-caloric effect of a $Gd_{50}Co_{50}$ amorphous alloy near the freezing point of water, AIP Adv., 5 (2015) 097122.

[5] L. Xia, Q. Guan, D. Ding, M.B. Tang, Y.D. Dong, Magneto-caloric response of the $Gd_{60}Co_{25}Al_{15}$ metallic glasses, Appl. Phys. Lett., 105 (2014) 192402.

[6] J. Schroers, Processing of bulk metallic glass, Adv. Mater., 22 (2010) 1566-1597.

[7] J. Plummer, W.L. Johnson, Is metallic glass poised to come of age?, Nat. Mater., 14 (2015) 553-555.

[8] F. Spaepen, Microscopic mechanism for steady-state inhomogeneous flow in metallic gasses, Acta Metall., 25 (1977) 407-415.

[9] A.L. Greer, Y.Q. Cheng, E. Ma, Shear bands in metallic glasses, Mater. Sci. Eng. R, 74 (2013) 71-132.

[10] S.F. Guo, J.L. Qiu, P. Yu, S.H. Xie, W. Chen, Fe-based bulk metallic glasses: Brittle or ductile?, Appl. Phys. Lett., 105 (2014) 161901.

[11] X.J. Gu, A.G. McDermott, S.J. Poon, G.J. Shiflet, Critical Poisson's ratio for plasticity in Fe-Mo-C-B-Ln bulk amorphous steel, Appl. Phys. Lett., 88 (2006) 211905.

[12] Y.J. Huang, J. Shen, J.F. Sun, Bulk metallic glasses: Smaller is softer, Appl. Phys. Lett., 90 (2007) 081919.

[13] N. Li, Q. Chen, L. Liu, Size dependent plasticity of a Zr-based bulk metallic glass during room temperature compression, J. Alloys Compd., 493 (2010) 142-147.

[14] T. Mukai, T.G. Nieh, Y. Kawamura, A. Inoue, K. Higashi, Effect of strain rate on compressive behavior of a $Pd_{40}Ni_{40}P_{20}$ bulk metallic glass, Intermetallics, 10 (2002) 1071-1077.

[15] H. Bei, S. Xie, E.P. George, Softening caused by profuse shear banding in a bulk metallic glass, Phys. Rev. Lett., 96 (2006) 105503.

[16] M.M. Trexler, N.N. Thadhani, Mechanical properties of bulk metallic glasses, Prog. Mater. Sci., 55 (2010) 759-839.

[17] R. Varadarajan, A.K. Thurston, J.J. Lewandowski, Increased toughness of zirconium-based bulk metallic glasses tested under mixed mode conditions, Metall. Mater. Trans. A, 41A (2010) 149-158.

[18] H.A. Hassan, J.J. Lewandowski, Effects of mixed mode loading on the fracture toughness of bulk metallic glass/W composites, Mater. Sci. Eng. A, 586 (2013) 413-417.

[19] P. Tandaiya, U. Ramamurty, R. Narasimhan, Mixed mode (I and II) crack tip fields in bulk metallic glasses, J. Mech. Phys. Solids, 57 (2009) 1880-1897.

[20] S.H. Chen, K.C. Chan, G. Wang, F.F. Wu, L. Xia, J.L. Ren, J. Li, K.A. Dahmen, P.K. Liaw, Loading-rate-independent delay of catastrophic avalanches in a bulk metallic glass, Sci. Rep., 6 (2016) 21967.

[21] H.A. Hassan, L. Kecskes, J.J. Lewandowski, Effects of changes in test temperature and loading conditions on fracture toughness of a Zr-based bulk metallic glass, Metall. Mater. Trans. A, 39A (2008) 2077-2085.

[22] P. Tandaiya, R. Narasimhan, U. Ramamurty, On the mechanism and the length scales involved in the ductile fracture of a bulk metallic glass, Acta Mater., 61 (2013) 1558-1570.

[23] R. Narasimhan, P. Tandaiya, I. Singh, R.L. Narayan, U. Ramamurty, Fracture in metallic glasses: mechanics and mechanisms, Int. J. Fracture, 191 (2015) 53-75.

[24] Z.F. Zhang, J. Eckert, L. Schultz, Difference in compressive and tensile fracture mechanisms of $Zr_{59}Cu_{20}Al_{10}Ni_8Ti_3$ bulk metallic glass, Acta Mater., 51 (2003) 1167-1179.

[25] Z.F. Zhang, G. He, J. Eckert, L. Schultz, Fracture mechanisms in bulk metallic

glassy materials, Phys. Rev. Lett., 91 (2003) 045505.

[26] K.M. Flores, R.H. Dauskardt, Mode II fracture behavior of a Zr-basred bulk metallic glass, J. Mech. Phys. Solids, 54 (2006) 2418-2435.

[27] R.T. Qu, M. Stoica, J. Eckert, Z.F. Zhang, Tensile fracture morphologies of bulk metallic glass, J. Appl. Phys., 108 (2010) 063509.

[28] Z.F. Zhang, R.T. Qu, J. Eckert, Tensile fracture criterion of metallic glass, J. Appl. Phys., 109 (2011) 083544.

[29] R.T. Qu, J.X. Zhao, M. Stoica, J. Eckert, Z.F. Zhang, Macroscopic tensile plasticity of bulk metallic glass through designed artificial defects, Mater. Sci. Eng. A, 534 (2012) 365-373.

[30] S.H. Chen, K.C. Chan, L. Xia, Effect of stress gradient on the deformation behavior of a bulk metallic glass under uniaxial tension, Mater. Sci. Eng. A, 574 (2013) 262-265.

[31] S.H. Chen, K.C. Chan, L. Xia, Deformation behavior of bulk metallic glass structural elements, Mater. Sci. Eng. A, 606 (2014) 196-204.

[32] J.X. Zhao, F.F. Wu, R.T. Qu, S.X. Li, Z.F. Zhang, Plastic deformability of metallic glass by artificial macroscopic notches, Acta Mater., 58 (2010) 5420-5432.

[33] S.H. Chen, K.C. Chan, L. Xia, Deformation behavior of a Zr-based bulk metallic glass under a complex stress state, Intermetallics, 43 (2013) 38-44.

[34] W.H. Wang, R.J. Wang, G.J. Fan, J. Eckert, Formation and properties of Zr-(Ti, Nb)-Cu-Ni-Al bulk metallic glasses, Mater. Trans., 42 (2001) 587-591.

[35] G. Wang, K.C. Chan, L. Xia, P. Yu, J. Shen, W.H. Wang, Self-organized intermittent plastic flow in bulk metallic glasses, Acta Mater., 57 (2009) 6146-6155.

[36] C.N. Kuo, H.M. Chen, X.H. Du, J.C. Huang, Flow serrations and fracture morphologies of Cu-based bulk metallic glasses in energy release perspective, Intermetallics, 18 (2010) 1648-1652.

[37] S.X. Song, H. Bei, J. Wadsworth, T.G. Nieh, Flow serration in a Zr-based bulk metallic glass in compression at low strain rates, Intermetallics, 16 (2008) 813-

818.

[38] R. Maaβ, D. Klaumunzer, J.F. Loffler, Propagation dynamics of individual shear bands during inhomogeneous flow in a Zr-based bulk metallic glass, Acta Mater., 59 (2011) 3205-3213.

[39] S.H. Chen, K.C. Chan, L. Xia, Fracture morphologies of Zr-based bulk metallic glasses under different stress states, Adv. Eng. Mater., 17 (2015) 366-373.

[40] W.D. Li, Y.F. Gao, H.B. Bei, Instability analysis and free volume simulations of shear band directions and arrangements in notched metallic glasses, Sci. Rep., 6 (2016) 34878.

[41] H.J. Leamy, H.S. Chen, T.T. Wang, Plastic-flow and fracture of metallic glass, Metall. Trans., 3 (1972) 699-708.

[42] C.A. Pampillo, A.C. Reimschuessel, The fracture topography of metallic glasses, J. Mater. Sci., 9 (1974) 718-724.

[43] C.T. Liu, L. Heatherly, D.S. Easton, C.A. Carmichael, J.H. Schneibel, C.H. Chen, J.L. Wright, M.H. Yoo, J.A. Horton, A. Inoue, Test environments and mechanical properties of Zr-base bulk amorphous alloys, Metall. Mater. Trans. A, 29 (1998) 1811-1820.

[44] F. Spaepen, On the fracture morphology of metallic glasses, Acta Metall., 23 (1975) 615-620.

[45] L.A. Deibler, J.J. Lewandowski, Model experiments to mimic fracture surface features in metallic glasses, Mater. Sci. Eng. A, 527 (2010) 2207-2213.

[46] L.A. Deibler, J.J. Lewandowski, Outer medium effects and fracture nucleation sites in model experiments to mimic fracture surface features of metallic glasses, Mater. Sci. Eng. A, 538 (2012) 259-264.

[47] M. Gao, B.A. Sun, C.C. Yuan, J. Ma, W.H. Wang, Hidden order in the fracture surface morphology of metallic glasses, Acta Mater., 60 (2012) 6952-6960.

[48] J. Hu, B.A. Sun, Y. Yang, C.T. Liu, S. Pauly, Y.X. Weng, J. Eckert, Intrinsic versus extrinsic effects on serrated flow of bulk metallic glasses, Intermetallics, 66 (2015) 31-39.

[49] B.A. Sun, S. Pauly, J. Tan, M. Stoica, W.H. Wang, U. Kuhn, J. Eckert, Serrated

flow and stick-slip deformation dynamics in the presence of shear-band interactions for a Zr-based metallic glass, Acta Mater., 60 (2012) 4160-4171.

[50] S.H. Chen, T.M. Yue, C.P. Tsui, K.C. Chan, Effect of external disturbances on the strain-rate dependent plastic deformation behavior of a bulk metallic glass, Mater. Sci. Eng. A, 669 (2016) 103-109.

[51] C.A. Schuh, T.G. Nieh, A nanoindentation study of serrated flow in bulk metallic glasses, Acta Mater., 51 (2003) 87-99.

[52] Z. Wang, J.W. Qiao, G. Wang, K.A. Dahmen, P.K. Liaw, Z.H. Wang, B.C. Wang, B.S. Xu, The mechanism of power-law scaling behavior by controlling shear bands in bulk metallic glass, Mater. Sci. Eng. A, 639 (2015) 663-670.

[53] J. Antonaglia, X. Xie, G. Schwarz, M. Wraith, J.W. Qiao, Y. Zhang, P.K. Liaw, J.T. Uhl, K.A. Dahmen, Tuned critical avalanche scaling in bulk metallic glasses, Sci. Rep., 4 (2014) 4382.

[54] X.L. Bian, G. Wang, K.C. Chan, J.L. Ren, Y.L. Gao, Q.J. Zhai, Shear avalanches in metallic glasses under nanoindentation: Deformation units and rate dependent strain burst cut-off, Appl. Phys. Lett., 103 (2013) 101907.

[55] K.A. Dahmen, Y. Ben-Zion, J.T. Uhl, A simple analytic theory for the statistics of avalanches in sheared granular materials, Nat. Phys., 7 (2011) 554-557.

[56] J.T. Uhl, S. Pathak, D. Schorlemmer, X. Liu, R. Swindeman, B.A.W. Brinkman, M. LeBlanc, G. Tsekenis, N. Friedman, R. Behringer, D. Denisov, P. Schall, X.J. Gu, W.J. Wright, T. Hufnagel, A. Jennings, J.R. Greer, P.K. Liaw, T. Becker, G. Dresen, K.A. Dahmen, Universal quake statistics: From compressed nanocrystals to earthquakes, Sci. Rep., 5 (2015) 16493.

[57] I. Regev, J. Weber, C. Reichhardt, K.A. Dahmen, T. Lookman, Reversibility and criticality in amorphous solids, Nat. Commun., 6 (2015) 8805.

[58] R. Carroll, C. Lee, C.W. Tsai, J.W. Yeh, J. Antonaglia, B.A.W. Brinkman, M. LeBlanc, X. Xie, S.Y. Chen, P.K. Liaw, K.A. Dahmen, Experiments and model for serration statistics in low-entropy, medium-entropy, and high-entropy alloys, Sci. Rep., 5 (2015) 16997.

[59] Y. Zhang, T.T. Zuo, Z. Tang, M.C. Gao, K.A. Dahmen, P.K. Liaw, Z.P. Lu,

Microstructures and properties of high-entropy alloys, Prog. Mater. Sci., 61 (2014) 1-93.

[60] J. Antonaglia, X. Xie, Z. Tang, C.W. Tsai, J.W. Qiao, Y. Zhang, M.O. Laktionova, E.D. Tabachnikova, J.W. Yeh, O.N. Senkov, M.C. Gao, J.T. Uhl, P.K. Liaw, K.A. Dahmen, Temperature effects on deformation and serration behavior of high-entropy alloys (HEAs), JOM, 66 (2014) 2002-2008.

[61] K.A. Dahmen, Y. Ben-Zion, J.T. Uhl, Micromechanical model for deformation in solids with universal predictions for stress-strain curves and slip avalanches, Phys. Rev. Lett., 102 (2009) 175501.

[62] J. Antonaglia, W.J. Wright, X.J. Gu, R.R. Byer, T.C. Hufnagel, M. LeBlanc, J.T. Uhl, K.A. Dahmen, Bulk metallic glasses deform via slip avalanches, Phys. Rev. Lett., 112 (2014) 155501.

[63] W.J. Wright, Y. Liu, X.J. Gu, K.D. Van Ness, S.L. Robare, X. Liu, J. Antonaglia, M. LeBlanc, J.T. Uhl, T.C. Hufnagel, K.A. Dahmen, Experimental evidence for both progressive and simultaneous shear during quasistatic compression of a bulk metallic glass, J. Appl. Phys., 119 (2016) 084908.

[64] J.J. Li, Z. Wang, J.W. Qiao, Power-law scaling between mean stress drops and strain rates in bulk metallic glasses, Mater. Design., 99 (2016) 427-432.

[65] S.H. Chen, T.M. Yue, C.P. Tsui, K.C. Chan, Flaw-induced plastic-flow dynamics in bulk metallic glasses under tension, Sci. Rep., 6 (2016) 36130.

[66] S.H. Chen, K.C. Chan, F.F. Wu, Pronounced energy absorption capacity of cellular bulk metallic glasses, Appl. Phys. Lett., 104 (2014) 111907.

[67] B. Sarac, J. Ketkaew, D.O. Popnoe, J. Schroers, Honeycomb structures of bulk metallic glasses, Adv. Funct. Mater., 22 (2012) 3160.

[68] S.H. Chen, K.C. Chan, T.M. Yue, F.F. Wu, Highly stretchable kirigami metallic glass structures with ultra-small strain energy loss, Scr. Mater., 142 (2018) 83-87.

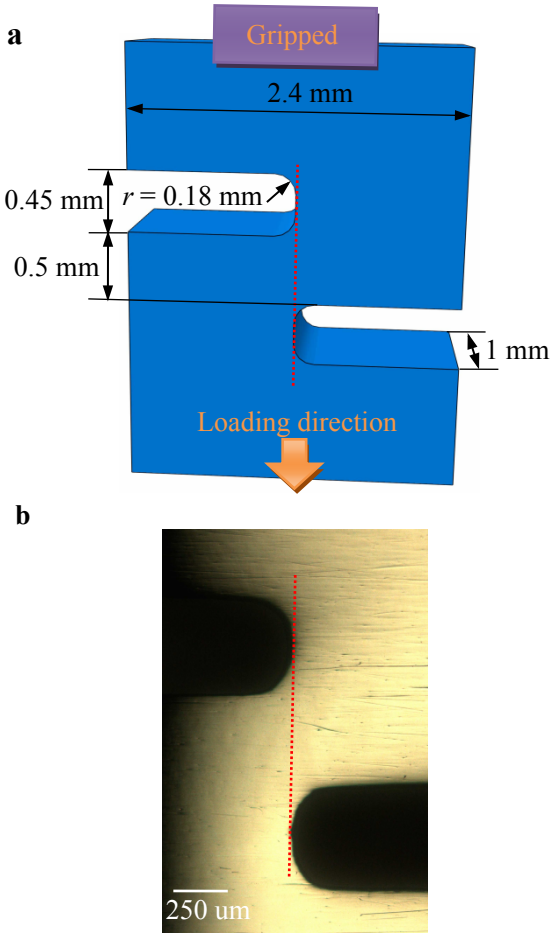

Fig. 1. Schematic diagram of the reduced section of the notched specimen (a), where (b) shows a prepared specimen.

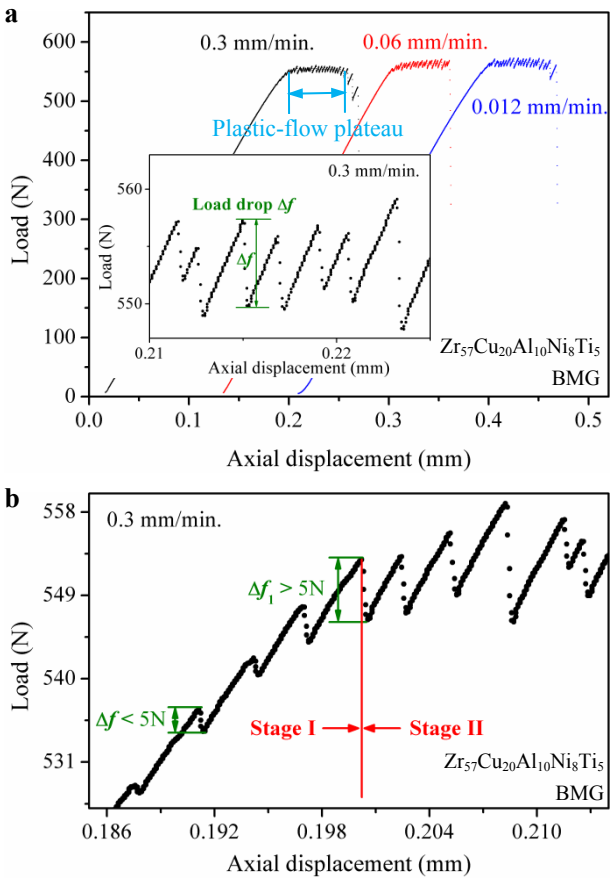

Fig. 2. (a) Tensile-testing results of the notched specimens at varying loading rates [20], where the inset shows an example of corresponding load drops (Δf) in the plastic-flow plateau. (b) Two stages of the plastic flow are determined by the first appearance of a load drop larger than 5 N (Δf_1), where at stage **I**, all load drops (Δf) are smaller than 5 N.

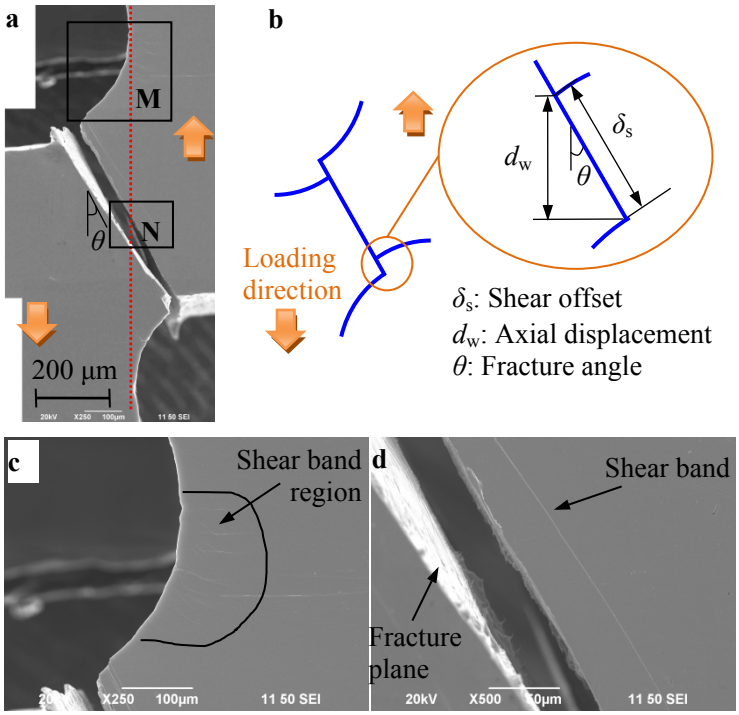

Fig. 3. (a) SEM image of a fractured specimen at a loading rate of 0.06 mm/min. (b) Schematic diagram showing the shear offset of the fractured specimen. (c,d) Magnified SEM images of regions, **M** and **N**, in (a), respectively.

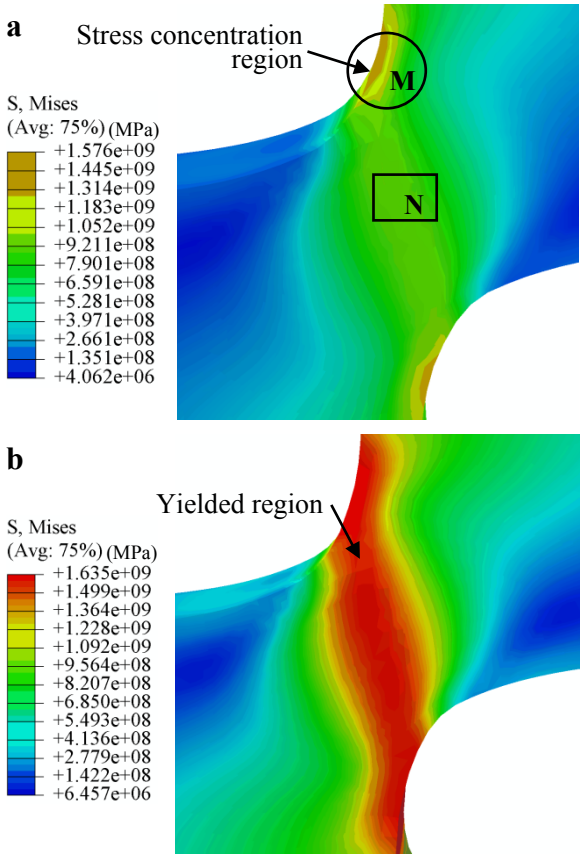

Fig. 4. FEM results showing the stress concentration around the notches, where (a) is in an elastic state, and (b) is after yielding. The regions, **M** and **N**, in (a) indicate the corresponding regions in Fig. 3a.

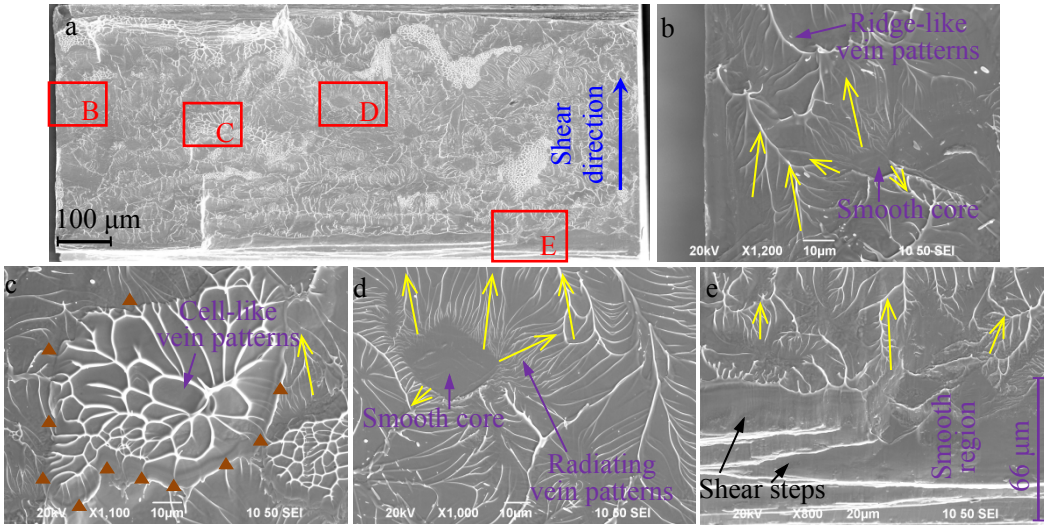

Fig. 5. Fracture-surface features of a specimen at a loading rate of 0.012 mm/min.. (a) The whole image of the fracture surface. (b-e) Magnified images of rectangles, B-E, in (a), respectively, where the yellow arrows indicate the propagation direction of the ridge-like vein patterns. (b) and (d) Ridge-like vein patterns and radiating veins co-existing with smooth cores at the side and center of the fracture surface, respectively. (c) Cell-like vein patterns, where the triangles indicate the boundary. (e) Smooth regions at different steps, which indicates that the fracture process consists of many slip events.

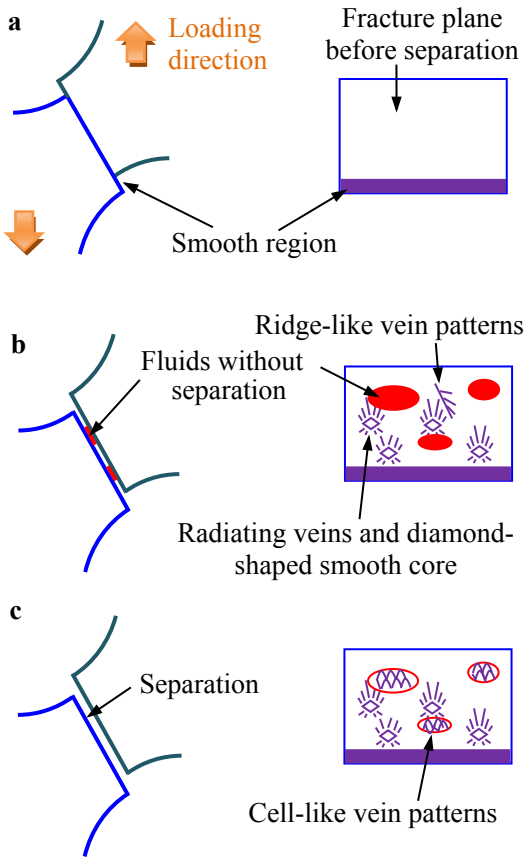

Fig. 6. Schematic diagram showing the formation of the fracture-surface features at three stages. (a) The formation of the smooth region during a shearing process. (b) The formation of ridge-like vein patterns, radiating veins and diamond-shaped smooth cores under a mixed mode I/II failure. (c) The formation cell-like vein patterns at a predominant-mode-II failure.

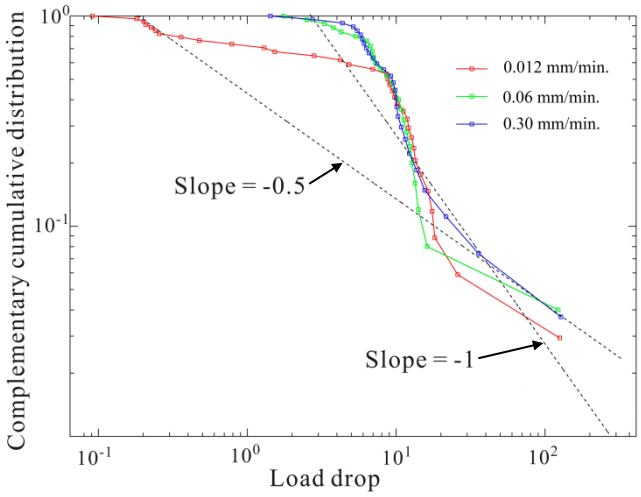

Fig. 7. Comparison with mean-field theory modeling of the complementary cumulative distribution functions (CCDF) of serration sizes (i.e., load-drop sizes) during plastic flow. The CCDF shows the probability of a stress drop on the y-axis to be larger than size S (on the x axis). The dashed lines with slopes of -0.5 and -1 indicate the predicted slopes of the slip-size distributions for brittle and ductile BMGs, respectively, for un-notched samples under uniaxial compression. The red, green, and blue curves show the CCDFs at different deformation rates for the experiment described here.